Catalysis Today 300 (2018) 112–123

Contents lists available at ScienceDirect

Catalysis Today

journal homepage: www.elsevier.com/locate/cattod

Novel synthesis of $PbBiO_2Cl$/BiOCl nanocomposite with enhanced visible-driven-light photocatalytic activity

Fu-Yu Liu[a], Yu-Rou Jiang[a], Chiing-Chang Chen[a,*], Wenlian William Lee[b,c,**]

[a] Department of Science Education and Application, National Taichung University of Education, Taichung 403, Taiwan
[b] Department of Occupational Safety and Health, Chung-Shan Medical University, Taichung 402, Taiwan
[c] Department of Occupational Medicine, Chung-Shan Medical University Hospital, Taichung 402, Taiwan

ARTICLE INFO

Keywords:
$PbBiO_2Cl$
BiOCl
Photocatalytic
Crystal violet
2-Hydroxybenzoic acid

ABSTRACT

The first synthetic study on $PbBiO_2Cl$/BiOCl nanocomposite preparation using a controlled hydrothermal method is reported. The composition and morphologies of the samples could be controlled by adjusting some growth parameters, including reaction pH, Pb/Bi molar ratio, and temperature. All the samples are characterized by XRD, TEM, XPS, SEM-EDS, FT-IR, BET, EPR, and UV–vis-DRS. The photodegradation activities are evaluated against the de-colorization of crystal violet (CV) and 2-hydroxybenzoic acid (2-HBA) in aqueous solution under visible light illumination. In particular, the catalytic performance illustrates the best reaction rate constant $2.763 \times 10^{-1}\,h^{-1}$ once $PbBiO_2Cl$/BiOCl is used as the photocatalyst for the degradation of CV; which is 3.01 and 2.12 times higher than the reaction rate constant of $PbBiO_2Cl$ and BiOCl being the photocatalysts, respectively. This study reveals that $PbBiO_2Cl$/BiOCl can be used for repressing the recombination of photo-generated electron-hole pairs and contribute to the enhanced photocatalytic activity of semiconductors in the visible-light-driven catalysis. The possible photocatalytic degradation mechanism is studied by using different active species through EPR and adding suitable scavengers. The results reveal that the reactive O_2^-, OH, h^+, $^1O_2$ play the major roles in the CV degradation.

1. Introduction

The elimination of toxic chemicals from wastewater has become one of the most crucial aspects of contemporary pollution-control methods because of the hazardous effects of these chemicals on living beings and the environment. In face of an increasingly serious environmental pollution and energy crunch, photocatalysis, as a suitable technology, plays an important role in the degradation of pollutants and solar energy conversion [1,2]. For the practical applications of photocatalysis, an environmentally powerful and cheap photocatalyst is an important component [3]. CV, a cationic triphenylmethane dye, was found the use as colorants in industry and as antimicrobial agents [4]. However, great trouble about the thyroid peroxidase-catalyzed oxidation of the triphenylmethane class of dyes was arisen because the reactions might produce various *N*-de-alkylated primary and secondary aromatic amines, with the structures similar to aromatic amine carcinogens [5]. Photocatalytic degradation of CV was studied using several systems to generate active species, including heterojunctions BiOI/g-C_3N_4 [6], BiOI/GO [7], $SrFeO_{3-x}$/g-C_3N_4 [8], BiOCl/BiOBr [9], BiOBr/$PbBiO_2Br$ [10], etc. and pure semiconductors $Bi_xAg_yO_z$ [11], Bi_2WO_6 [12], TiO_2 [13], etc. As shown in Table 1, mixed oxide based photocatalysts have obtained remarkable interests in recent years because of their suitable band gaps, stability, and relatively superior photocatalytic activities. It is found that the mixed oxide based photocatalysts shows higher photocatalytic activities than pure metal oxide based photocatalysts for the photocatalytic degradation of remediation [8–10,12–15].

During the last two decades, besides the focused work on TiO_2 modifications, many efforts were made to develop other novel efficient photocatalysts [16–19]. Recently, Bi-based oxychlorides have drawn our attentions to their potential application as novel photocatalysts owing to their unique layered structures and high chemical stabilities [13,20,21]. The original Bi-based oxychlordie is the Sillén family expressed by $[M_2O_2][Cl_m]$ (m = 1–3) [22,23] where bismuth oxide-based fluorite-like layers, $[M_2O_2]$, are inter-grown with single, double, or triple chlorine layers to construct such compositions as $PbBiO_2Cl$, BiOCl, et al. Sillen's phases are an adaptive structure series of oxyhalides originally investigated by Sillen and co-workers in the 1940's [24]. The structures of these compounds consist of $[M_2O_2]$ layers (M = Pb, Bi, Cd, Ba, Sr) intermixed with either halogen or metal

* Corresponding author.
** Corresponding author at: Department of Occupational Safety and Health, Chung-Shan Medical University, Taichung 402, Taiwan.
E-mail addresses: ccchen@mail.ntcu.edu.tw, ccchen@ms3.ntcu.edu.tw (C.-C. Chen), wllee01@gmail.com (W.W. Lee).

http://dx.doi.org/10.1016/j.cattod.2017.04.030
Received 31 August 2016; Received in revised form 27 March 2017; Accepted 13 April 2017
Available online 26 April 2017
0920-5861/

Table 1
Photocatalytic properties of mixed oxide based photocatalysts for the degradation of remediation under visible light irradiation.

Mixed oxide based photocatalyst	Mass fraction of mixed oxide (%)	Parameters of photocatalytic experiments	Photocatalytic activity	Reference Photocatalyst/ photocatalytic activity	Enhancement factor	Reference
$SrFeO_{3-x}/g\text{-}C_3N_4$	4	Crystal violet Chloramphenicol	95% decomposition in 24 h 97% decomposition in 24 h	g-C_3N_4: 21% $SrFeO_{3-x}$: 1%	– 4.77 4.8	[8]
$Bi_3O_4Cl/Bi_{24}O_{31}Br_{10}$	–	Crystal violet	99% in 48 h	–	–	[9]
$PbBiO_2Br/BiOBr$	–	Crystal violet	98% in 72 h.	$PbBiO_2Br$: 33% BiOBr: 50%	3 2	[10]
$SrBiO_2Br$	5%	Rhodamine B	68% in 12 h.	–	– 7.3	[13]
F-Bi_2MoO_6	20%F	Rhodamine B Phenol Bisphenol A 4-Chlorophenol	88.0% in 100 min. 45.3% in 100 min. 74.7% in 100 min. 33.6% in 100 min.	Bi_2MoO_6: 30% Bi_2MoO_6: 11.2% Bi_2MoO_6: 33% Bi_2MoO_6: 53%	3.5 8.9 3.0 1.9	[15]
$PbBiO_2I$	–	Nitrobenzene	4%	–	–	[14]
Bi_2WO_6	–	Crystal violet	92.1% in 24 h	–	–	[12]

halogen layers. Two examples of these phases are BiOCl and $PbBiO_2Cl$ which consist of $[M_2O_2]$ + 2 halogen and $[M_2O_2]$ + 1 halogen layers respectively. The Aurivillius intergrowth phases consist of perovskite blocks sandwiched between the $[Bi_2O_2]^{2+}$ slabs and can be described with a general formula $[Bi_2O_2]$- $A_{n-1}B_nO_{3n+1}$, where A is a large alkali, alkali-earth, rare-earth, or Pb^{2+} cation, and B is a d^0 transition metal cation, such as Nb^{5+}, W^{6+}, Ta^{5+}, or Ti^{4+} [25]. The extended Bi-based oxychlorides are the Sille'n–Aurivillius intergrowth $[Bi_2O_2][A_{n-1}B_nO_{3n+1}][Bi_2O_2][Cl_m]$ [13,21] where the Aurivillius family $[Bi_2O_2][A_{n-1}B_nO_{3n+1}]$ is intergrown with the structure-similarity Sillén family $[Bi_2O_2][Cl_m]$, $X_m]$, where n is the number of perovskite layers and m is the number of halide layers, such as Bi_4TaO_8Cl, Bi_4NbO_8Cl, etc. These oxychloride compounds are of interest as selective oxidation catalysts [13], ferroelectric materials [21] and pigments [26].

Bi-based layered structure compounds, within Aurivillius family, such as Bi_2WO_6 [27], $Bi_4Ti_3O_{12}$ [28], $BiVO_4$ [29], BiOX (X = Cl, Br, I) [9,30–32], etc., have been extensively explored as highly efficient photo-catalysts due to their unique layered structure and high catalytic activity. It is thought that the Bi 6 s and O 2p levels can make a largely dispersed hybridized valence band, which favors the mobility of photo-generated holes and the oxidation reaction, inducing efficient separation of photo-generated electron-hole pairs and then improving the photo-catalytic efficiency [33]. Many inorganic materials have modular structures, where individual units are responsible for different functions. The $[Bi_2O_2]^{2+}$ slabs with the α-PbO type structure as well as simple halide layers are effective spacers in some layered functional materials [25]. Previous reports discussed mainly electronic reasons for the different photocatalytic activity of layered $PbBiO_2X$-type materials (X = Cl, Br, I) [10,14,34–36]. However, crystal-chemical arguments should also be taken into consideration to explain the photocatalytic properties of the compounds. A possible reason for the different catalytic activity of the oxides may be derived collectively from their crystal structures, their optic, and their redox properties. All the solid materials under discussion crystallize in a layered structure. They exhibit covalent metal oxygen layers $[PbBiO_2]^+$ separated by halide layers, which are stacked along [001]. One can assume that the crystal surface consists of metal oxygen layers, i.e., the metal atoms are expected to form the (001) surfaces. In the case of bismuth compounds, the metal position was statistically occupied by lead and bismuth with the ratio 1:1 [37,38]. It was reported that the band gaps of $PbBiO_2I$ [14], $PbBiO_2Br$ [10,34], and $PbBiO_2Cl$ [35] were 2.39, 2.47, and 2.53 eV, respectively. It seemed that the gaps of all these semiconductors were in the visible-light range to catalyze the photocatalytic reaction.

Recently, the development of visible-light-driven photocatalysts has obtained considerable attention as an alternative in wastewater treatment. An effective and simple tactic to improve the photocatalytic activity of a photocatalyst is the incorporation of a heterostructure, because heterojunctions have great potential for tuning the wished electronic properties of photocatalysts and efficiently separating the photogenerated electron–hole pairs [39–41]. So far, a heterojunction concerned $PbBiO_2Br$, such as $PbBiO_2Br/BiOBr$ and $PbBiO_2Br/NbSe_2$, has been reported and exhibited the enhanced photocatalytic efficiency [10,42]. Therefore, it is feasible for $PbBiO_2Br$ being partly transformed into $NbSe_2$ via a thermodynamically favored direction through the ion exchange reaction, which allows the exchange between the component ions and the incoming species [43], to consequently obtain the $PbBiO_2Br/NbSe_2$ heterojunction.

To the best of our knowledge, nanocomposite semiconductors consisting of $PbBiO_2Cl$ and BiOCl have not yet been reported in the literature. This is the first report that $PbBiO_2Cl/BiOCl$ composites are prepared by a template-free hydrothermal method. Through degrading CV and 2-HBA in aqueous solution under visible-light irradiation, the photocatalytic activities of $PbBiO_2Cl/BiOCl$ composites are further discussed.

2. Experimental details

2.1. Materials

$Pb(NO_3)_2{\cdot}H_2O$, ammonium oxalate (Osaka), 2-hydroxybenzoic acid (salicylic acid), $Bi(NO_3)_3{\cdot}5H_2O$ (Katayama), CV dye (TCI), *p*-benzoquinone (Alfa aesar), sodium azide (Sigma-Aldrich), and isopropanol (Merck) were purchased and used without further purification. Reagent-grade HNO_3, NaOH, CH_3COONH_4, and HPLC-grade methanol were obtained from Merck.

2.2. Instruments and analytical methods

The Brunauer-Emmett-Teller (BET) specific surface areas of the samples (S_{BET}) were measured with an automated system (Micrometrics Gemini) using nitrogen gas as the adsorbate at liquid nitrogen temperature. The field-emission transmission electron microscopy (FE-TEM) images, selected area electron diffraction (SAED) patterns, high resolution transmission electron microscopy (HRTEM) images, and energy-dispersive X-ray spectra (EDS) were obtained using JEOL-2010 with an accelerating voltage of 200 kV. The X-ray diffraction (XRD) patterns were recorded on a MAC Science MXP18 equipped with Cu-Kα radiation, operating at 40 kV and 80 mA. Field emission scanning electron microscopy-electron dispersive X-ray spectroscopy (FE-SEM-EDS) measurements were carried out using a JEOL JSM-7401F at an acceleration voltage of 15 kV. The Al-Kα radiation was generated at 15 kV. High resolution X-ray photoelectron spectroscopy (HRXPS)

measurements were carried out using ULVAC-PHI. The Ultra-violet photoelectron spectroscopy (UPS) measurements were performed using ULVAC-PHI XPS, PHI Quantera SXM. Waters ZQ LC/MS system, equipped with a binary pump, a photodiode array detector, an autosampler, and a micromass detector, was used for separation and identification. The amount of residual dye at each reaction cycle was determined by HPLC–MS. The analysis of organic intermediates was accomplished by HPLC–MS after readjustment of chromatographic conditions in order to make the mobile phase (Solvent A and B) compatible with the working conditions of the mass spectrometer. Solvent A was 25 mM aqueous ammonium acetate buffer (pH 6.9), and solvent B was methanol. LC was carried out on an Atlantis ™ dC18 column (250mm × 4.6 mm i.d., dp = 5 μm). The mobile phase flow rate was 1.0 mL/min. A linear gradient was run as follows: t = 0, A = 95, B = 5; t = 20, A = 50, B = 50; t = 35–40, A = 10, B = 90; t = 45, A = 95, B = 5. The column effluent was introduced into the ESI source of the mass spectrometer.

2.3. Synthesis of $PbBiO_2Cl$/BiOCl

1, 3 mmol $Pb(NO_3)_2{\cdot}H_2O$ and 3 mmol $Bi(NO_3)_3{\cdot}5H_2O$ were first mixed in a 50 mL flask, and followed by adding 30 mL H_2O. With continuous stirring, 2 M NaOH was added dropwise to adjust the pH = 1–14. The solution was then stirred vigorously for 30 min and 10 mL solution was transferred into a 30 mL Teflon-lined autoclave, which was heated up to 100–250 °C for 12 h and then naturally cooled down to room temperature. These resulted solid precipitate was collected by filtration, washed with deionized water and methanol to remove any possible ionic species in the solid precipitate, and then dried at 60 °C overnight. Depending on the $Pb(NO_3)_2{\cdot}H_2O$/$Bi(NO_3)_3{\cdot}5H_2O$ molar ratio (1:3, 3:3), pH value, temperature, and reaction time, the samples were synthesized and labeled as shown in Table 2; the as-prepared samples were labeled from P1BC1-150-1-12 to P3BC1-250-13-12

2.4. Photocatalytic experiments

The CV irradiation experiments were carried out on stirred aqueous solution contained in a 100-mL flask; the aqueous suspension of CV (100 mL, 10 ppm) and the amount of catalyst powder were placed in a Pyrex flask. The pH of the suspension was adjusted by adding either NaOH or HNO_3 solution. Dark experiments were performed in order to examine the adsorption/desorption equilibrium. 10 mg of the photocatalyst was mixed with 100 mL CV aqueous solution with a known initial concentration in a 100 mL flask and the mixture was shaken in an orbital shaker (100 rpm) at a constant temperature. The mixture was centrifuged at 3000 rpm in a centrifugation machine after batch sorption experiments so that the absorbance of CV could be determined at 580 nm by means of HPLC–MS. The concentrations of the solutions were determined using linear regression equation. Prior to the irradiation, the suspension was magnetically stirred in dark for ca. 30 min to establish an adsorption/desorption equilibrium between the CV and the catalyst surface. Irradiation was carried out using 150 W Xe arc lamps, the light intensity was fixed at 31.2 W/m^2, and the reaction vessel was placed 30 cm away from the light source. At given irradiation time intervals, a 5-mL aliquot was collected and centrifuged to remove the catalyst. The supernatant was measured by HPLC–MS.

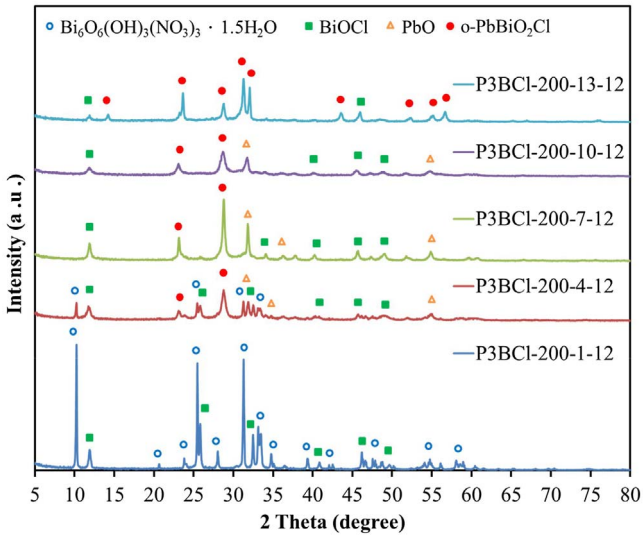

Fig. 1. XRD patterns of as-prepared samples under different pH values, at reaction temperature 200 °C and reaction time 12 h. (Molar ratio $Pb(NO_3)_2/Bi(NO_3)_3$ = 3/3, KCl = 1 mmol).

A different quencher was introduced to scavenge the relevant active species in order to evaluate the effect of the active species during the photocatalytic reaction. Active species, ·OH, $O_2{\cdot}^-$, h^+, and $^1O_2$, were studied by adding 1.0 mM isopropanol (IPA, a quencher of ·OH) [44], 1.0 mM benzoquinone (BQ, a quencher of $O_2{\cdot}^-$) [45], 1.0 mM ammonium oxalate (AO, a quencher of h^+) [46], and 1.0 mM sodium azide (SA, a quencher of $^1O_2$ [47], respectively. The method was similar to the former photocatalytic experiments [7,8].

3. Results and discussion

3.1. Characterization of as-prepared samples

3.1.1. XRD

Figs. 1 and S1–S5 show the XRD patterns of the as-prepared samples; the patterns clearly show the existence of the composites, *o*-$PbBiO_2Cl$/BiOCl, *t*-$PbBiO_2Cl/Bi_2O_3$, BiOCl/$Bi_6O_6(OH)_3(NO_3)_3{\cdot}1.5H_2O$, *o*-$PbBiO_2Cl$/PbO/BiOCl, PbO/BiOCl/$Bi_6O_6(OH)_3(NO_3)_3{\cdot}1.5H_2O$, and *o*-$PbBiO_2Cl$/PbO/BiOCl/$Bi_6O_6(OH)_3(NO_3)_3{\cdot}1.5H_2O$. Table 3 summarizes the results of the XRD measurements. All the samples as-prepared contain *o*-$PbBiO_2Cl$ phase (JCPDS 075-2095), *t*-$PbBiO_2Cl$ phase (JCPDS 039-0802), BiOCl phase (JCPDS 085-0861), PbO phase (JCPDS 085-1287), $Bi_6O_6(OH)_3(NO_3)_3{\cdot}1.5H_2O$ phase (JCPDS 053-1038), and Bi_2O_3 (JCPDS 71-0465).

Table 2
Codes of as-prepared samples under different hydrothermal conditions. ($Pb(NO_3)_2/Bi(NO_3)_3$ = 1/3–3/3, KCl = 1 mmol, pH = 1–13, temp = 150–250 °C, time = 12 h).

Temperature (°C)/ Molar ratio (Pb:Bi)	pH value				
	1	4	7	10	13
150(1:3)	P1BCl-150-1-12	P1BCl-150-4-12	P1BCl-150-7-12	P1BCl-150-10-12	P1BCl-150-13-12
150(3:3)	P3BCl-150-1-12	P3BCl-150-4-12	P3BCl-150-7-12	P3BCl-150-10-12	P3BCl-150-13-12
200(1:3)	P1BCl-200-1-12	P1BCl-200-4-12	P1BCl-200-7-12	P1BCl-200-10-12	P1BCl-200-13-12
200(3:3)	P3BCl-200-1-12	P3BCl-200-4-12	P3BCl-200-7-12	P3BCl-200-10-12	P3BCl-200-13-12
250(1:3)	P1BCl-250-1-12	P1BCl-250-4-12	P1BCl-250-7-12	P1BCl-250-10-12	P1BCl-250-13-12
250(3:3)	P3BCl-250-1-12	P3BCl-250-4-12	P3BCl-250-7-12	P3BCl-250-10-12	P3BCl-250-13-12

Table 3
Crystalline phase changes of as-prepared samples under different hydrothermal conditions. ($Pb(NO_3)_2/Bi(NO_3)_3$ = 1/3–3/3, KCl = 1 mmol, pH = 1–14, temp = 150–250 °C, time = 12 h).

Temperature (°C) /	pH value				
Molar ratio (Pb:Bi)	1	4	7	10	13
150(1:3)	■○	■○△	■○△	■○△	▲○
150(3:3)	■○	■○△●	■△●	■△●	■●
200(1:3)	■○	■○△	■○△	■△	▲○
200(3:3)	■○	■○△●	■△●	■△●	■●
250(1:3)	■○	■○△	■△	■△	▲○
250(3:3)	■○	■○△●	■△●	■△●	■●

■ :BiOCl ○ :$Bi_6O_6(OH)_3(NO_3)_3 \cdot 1.5H_2O$ △ :PbO ○ :*t*-$PbBiO_2Cl$ ▲ :Bi_2O_3 ● : *o*-$PbBiO_2Cl$

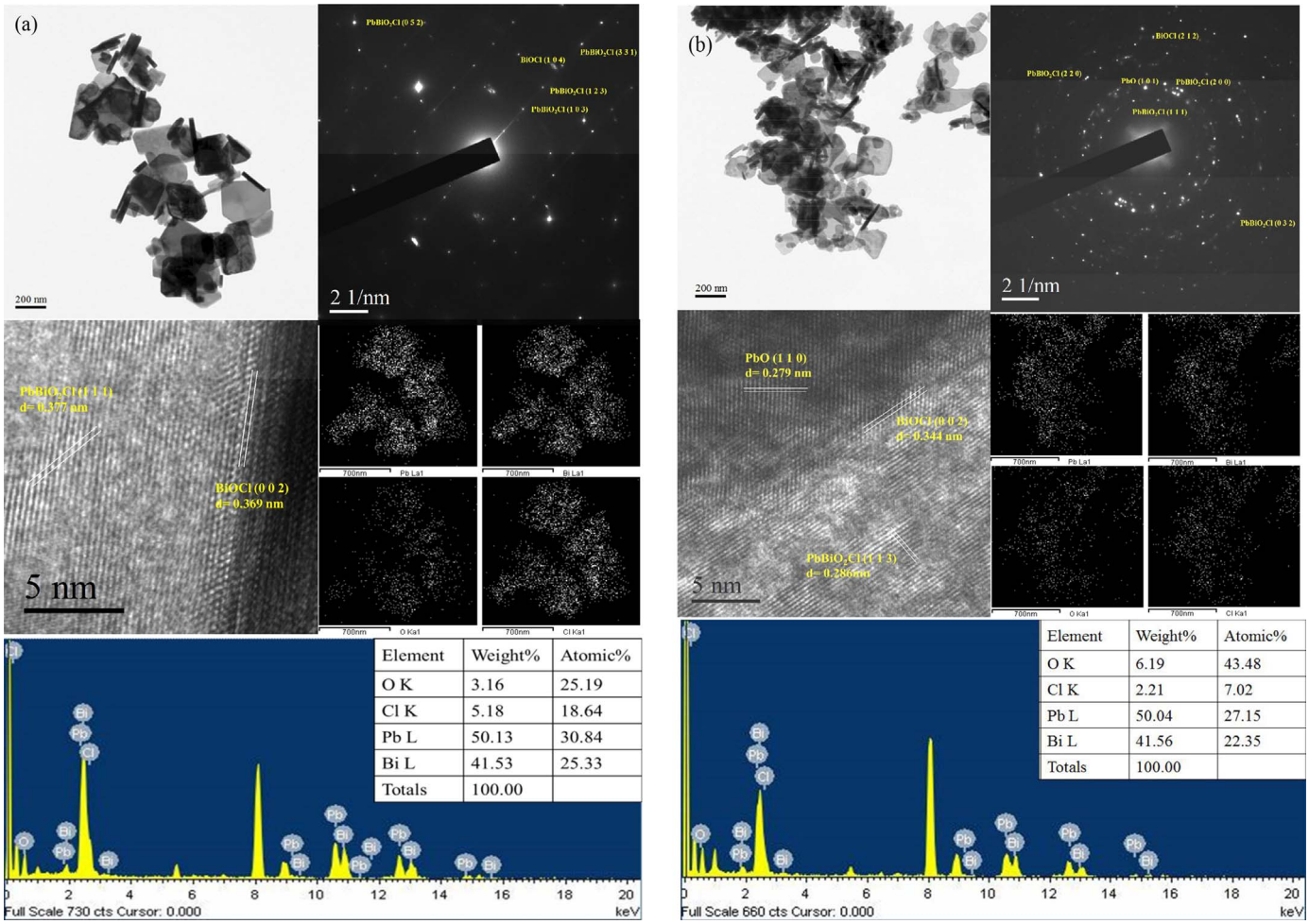

Fig. 2. FE-TEM images, SAD, mapping, and EDS of (a) BiOCl/o-$PbBiO_2Cl$ (P3BCl-200-13-12), and (b) BiOCl/PbO/o-$PbBiO_2Cl$ (P3BCl-250-10-12) samples by the hydrothermal autoclave method.

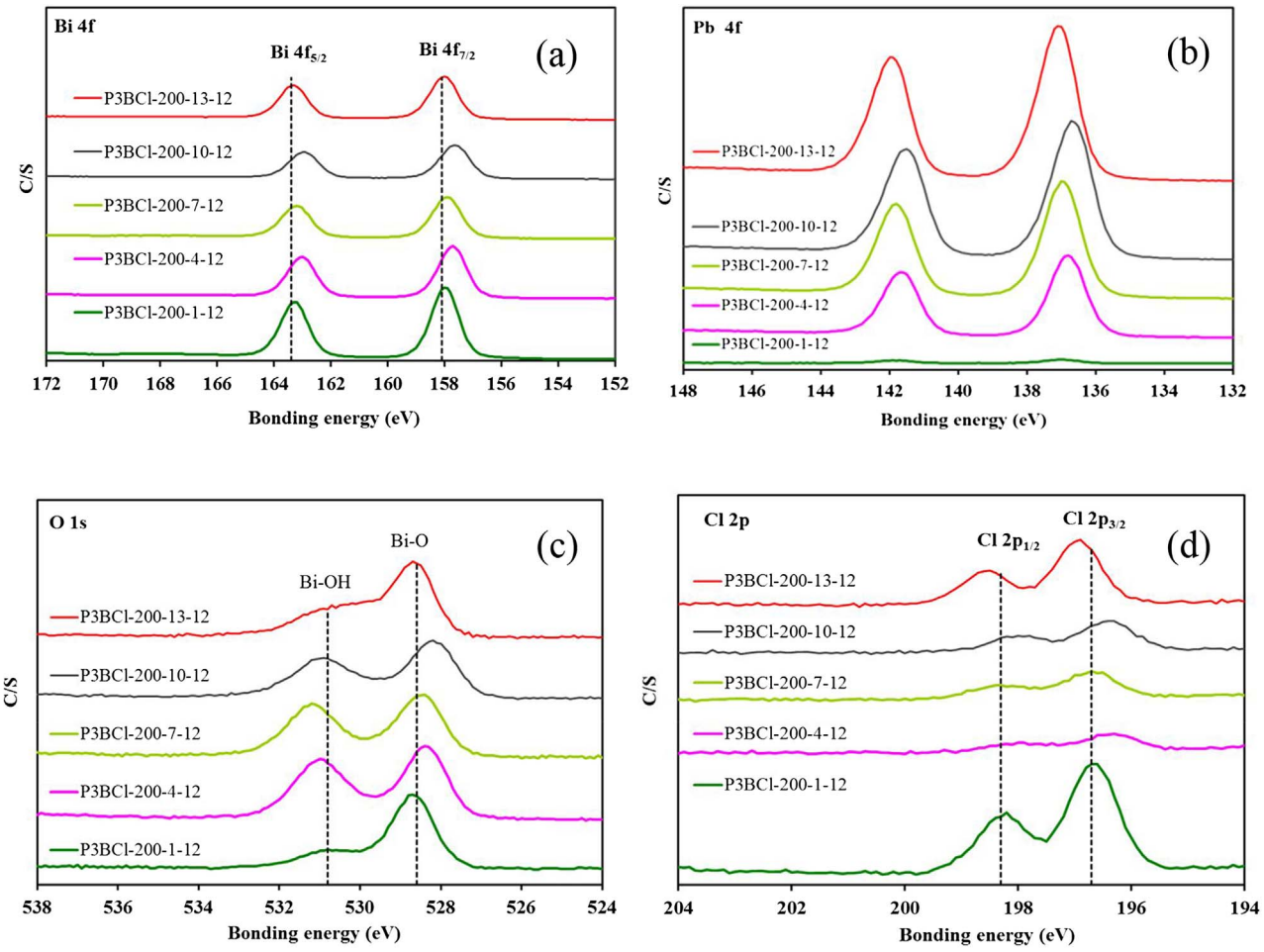

Fig. 3. XPS spectra of as-prepared samples under different pH values, at reaction temperature 200 °C and reaction time 12 h. (Molar ratio $Pb(NO_3)_2/Bi(NO_3)_3$ = 3/3, KCl = 1 mmol). (a) Bi 4f, (b) Pb 4f, (c) O 1s, (d) Cl 2p.

3.1.2. TEM

Fig. 2 displays that *o*-$PbBiO_2Cl$/BiOCl and *o*-$PbBiO_2Cl$/PbO/BiOCl are composed of different-size layers, consistent with the TEM observations. In addition, the EDS spectrum shows that the sample contains the elements of Bi, Pb, Cl, and O. In Fig. 2(a), the HRTEM image demonstrates that two sets of lattice images are obtained with d-spacings of 0.377 and 0.369 nm, corresponding to the (111) plane of *o*-$PbBiO_2Cl$ and the (002) plane of BiOCl, and the d-spacings of 0.286, 0.279, and 0.344 nm corresponded to the (113) plane of *o*-$PbBiO_2Cl$, the (110) plane of PbO, and the (002) plane of BiOCl (Fig. 2(b)), respectively, which is in strong agreement with the XRD results. The results suggest that the *o*-$PbBiO_2Cl$/BiOCl and *o*-$PbBiO_2Cl$/PbO/BiOCl phases have been formed in the composites, which are favorable for the separation of photoinduced carriers, yielding high photocatalytic activities.

3.1.3. XPS

Fig. 3 presents the Bi 4f, Pb 4f, O 1s, and Cl 2p XPS spectra of the *o*-$PbBiO_2Cl$/BiOCl composites. Observation of the transition peaks involving the Bi 4f, Pb 4f, O 1s, and Cl 2p orbitals identifies that the catalysts are composed of Bi, Pb, O, and Cl. The characteristic binding energy value 158.0 eV for Bi $4f_{7/2}$ (Fig. 3(a)) shows a trivalent oxidation state for bismuth. A similar chemical binding for Bi $4f_{7/2}$ was also reported by Liao et al. [48]. From Fig. 3(b), the binding energy 136.9-137.5 eV is attributed to Pb $4f_{7/2}$ respectively, which could be pointed to Pb at the divalent oxidation state [49]. Kovalev et al. demonstrated that the particle size of PbS could be correlated with observable changes in the binding energy of the Pb XPS peak. They reported that relative integral intensity of the peak depended upon the fraction of particle in the specific region [50,51], which indicated that higher successive ionic layer adsorption and reaction cycle led to the formation of the fraction of bigger and smaller particles on the surface of titania nanotube. The $4f_{5/2}$ peak observed at 137.8 and 138.9 eV is due to the presence of two different particle sizes of PbS formed in TiO_2 nanotube arrays. The asymmetric O 1s peak shown in Fig. 3(c) can be split by using the XPS peak-fitting program. The peak at 530.4 eV is assigned to the external −OH group or the water molecule adsorbed on the surface, and the other O 1s peak appearing at 528.8 eV corresponds to lattice oxygen atoms in $PbBiO_2Br$/BiOBr [32]. From Fig. 3(d), the binding energy of 196.8–197.0 eV and 198.3-198.6 eV is referred to Cl $2p_{3/2}$ and Cl $2p_{1/2}$ respectively which can be assigned to Cl at the monovalent oxidation state. These results agree with those of XRD and TEM experiment.

According to earlier studies [48,52,53], a series of bismuth oxybromides in the formation process were reported by Chen et al. The proposed processes for the formation of *o*-$PbBiO_2Cl$/BiOCl and *o*-$PbBiO_2Cl$/PbO/BiOCl composites are described in equations 1–10. The results demonstrate a series of changes in the compounds prepared at different hydrothermal conditions, described as $BiOCl \rightarrow Bi_4O_5Cl_2 \rightarrow Bi_{24}O_{31}Cl_{10} \rightarrow Bi_3O_4Cl \rightarrow Bi_5O_7Cl \rightarrow Bi_{12}O_{17}Cl_2 \rightarrow Bi_2O_3$, $PbCl_2 \rightarrow Pb(OH)Cl \rightarrow PbBiO_2Cl$, and $PbCl_2 \rightarrow Pb(OH)_2 \rightarrow PbO$. By controlling the pH of the hydrothermal reaction, different compositions are obtained as follows.

$$Bi^{3+} + 3OH^- \rightarrow Bi(OH)_{3(s)} \quad (1)$$

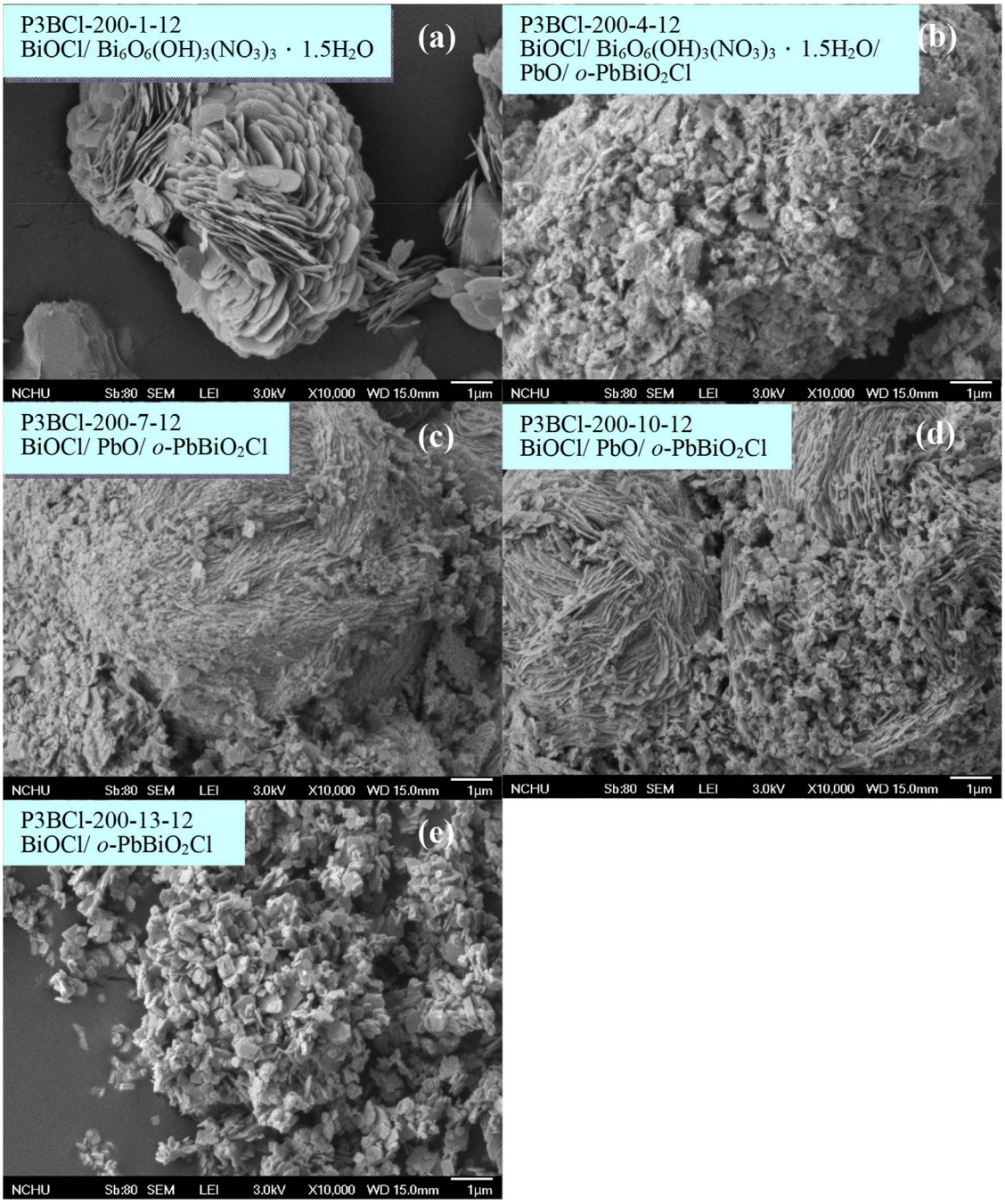

Fig. 4. SEM images of as-prepared samples by the hydrothermal autoclave method at different pH values. (Molar ratio $Pb(NO_3)_2/Bi(NO_3)_3$ = 3/3, KCl = 1 mmol, hydrothermal conditions: pH = 1–13, temp = 200 °C, time = 12 h).

$$12Bi(OH)_{3(s)} + 6HNO_3 \rightarrow 2[Bi_6O_6(OH)_3(NO_3)_3{\cdot}1.5H_2O] \quad 2[Bi_6O_6(OH)_3(NO_2[Bi_6O_6(OH)_3(NO_3)_3{\cdot}1.5H_2O]_3)_3{\cdot}1{\cdot}5H_2O]_{(s)} + 15H_2O \quad (2)$$

$$2Bi(OH)_{3(s)} + Cl^- \rightarrow BiOCl_{(s)} + H_2O + OH^- \quad (3)$$

$$Bi^{3+} + 3Cl^- \rightarrow BiCl_{3(s)} \quad (4)$$

$$BiCl_{3(s)} + 2OH^- \rightarrow BiOCl_{(s)} + 2Cl^- + H_2O \quad (5)$$

$$Pb^{2+} + 2Cl^- \rightarrow PbCl_{2(s)} \quad (6)$$

$$PbCl_{2(s)} + OH^- \rightarrow Pb(OH)Cl_{(s)} \quad (7)$$

$$Pb(OH)Cl_{(s)} + 2OH^- \rightarrow Pb(OH)_2 \quad (8)$$

$$BiOCl_{(s)} + Pb(OH)_2 \rightarrow PbBiO_2Cl_{(s)} + H_2O \quad (9)$$

$$Pb(OH)_2 \rightarrow PbO_{(s)} + H_2O \quad (10)$$

3.1.4. Morphological structure and composition

Figs. 4 and S5–S9 show the FESEM images of the composites *o*-$PbBiO_2Cl$/BiOCl, *t*-$PbBiO_2Cl/Bi_2O_3$, BiOCl/$Bi_6O_6(OH)_3(NO_3)_3{\cdot}1.5H_2O$, *o*-$PbBiO_2Cl$/PbO/BiOCl, PbO/BiOCl/$Bi_6O_6(OH)_3(NO_3)_3{\cdot}1.5H_2O$, and *o*-$PbBiO_2Cl$/PbO/BiOCl/$Bi_6O_6(OH)_3(NO_3)_3{\cdot}1.5H_2O$ at high magnification, respectively. From the observations, *o*-$PbBiO_2Cl$, *t*-$PbBiO_2Cl$, PbO, BiOCl, $Bi_6O_6(OH)_3(NO_3)_3{\cdot}1.5H_2O$ samples show square-plate, thin-square-plate, rod, nano-thin-sheet (or flower-like), and irregular-

Table 4
XPS and EDS of as-prepared samples prepared under different reaction conditions. (Pb$(NO_3)_2$/Bi$(NO_3)_3$ = 1/3–3/3, KCl = 1 mmol, pH = 1–14, temp = 150–250 °C, time = 12 h).

Sample code	XPS of atomic ratio (%)				EDS of atomic ratio (%)			
	Pb	Bi	O	Cl	Pb	Bi	O	Cl
P3BCl-200-1-12	0.5	36.6	42.7	20.2	0.15	33.21	37.08	29.56
P3BCl-200-4-12	10.5	25.5	51.1	12.9	7.18	23.24	58.77	10.80
P3BCl-200-7-12	16.2	21.9	56.8	5.1	8.49	20.60	65.01	5.89
P3BCl-200-10-12	21.3	19.0	53.7	6.1	12.98	16.50	64.95	5.57
P3BCl-200-13-12	22.9	17.9	52.8	6.5	15.33	13.63	58.46	12.58

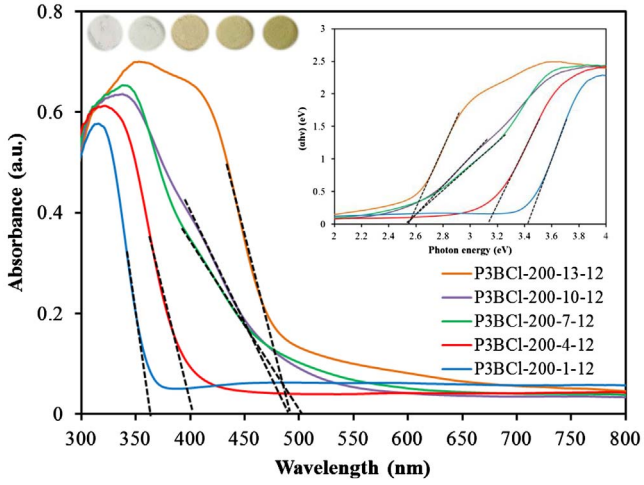

Fig. 5. UV–vis absorption spectra of the as-prepared photocatalysts under different pH values. (Molar ratio Pb$(NO_3)_2$/Bi$(NO_3)_3$ = 3/3, KCl = 1 mmol, reaction temp = 200 °C, reaction time 12 h).

nanosheet morphology, respectively. The SEM-EDS results demonstrate that the main elements within these samples are lead, bismuth, oxygen, and chlorine at Table 4 and Table S1. From above results, the composites could be selectively synthesized through a controlled hydrothermal method.

3.1.5. Optical absorption properties

As shown in Figs. 5 and S10–S14 for DR-UV of the as-prepared samples, the absorption edge of the samples are around 362.5–505.1 nm, which originates from its band gap of 2.50–3.42 eV (Table 5) and is consistent with the reported results [34,48]. Pure

Table 5
Physical and chemical properties of as-prepared samples at different pH value. (Pb$(NO_3)_2$/$BiBr_3$ = 3/3, pH = 1–14, temp = 200 °C, time = 12 h).

Samples	S_{BET} ($m^2\,g^{-1}$)	Pore volume ($cm^3\,g^{-1}$)	Pore diameter (nm)	Band gap (eV)
P3BCl-200-1-12	2.67	0.03	52.96	3.42
P3BCl-200-4-12	14.74	0.19	51.80	3.18
P3BCl-200-7-12	9.80	0.12	84.79	2.50
P3BCl-200-10-12	12.41	0.20	84.98	2.52
P3BCl-200-13-12	3.04	0.06	144.35	2.57

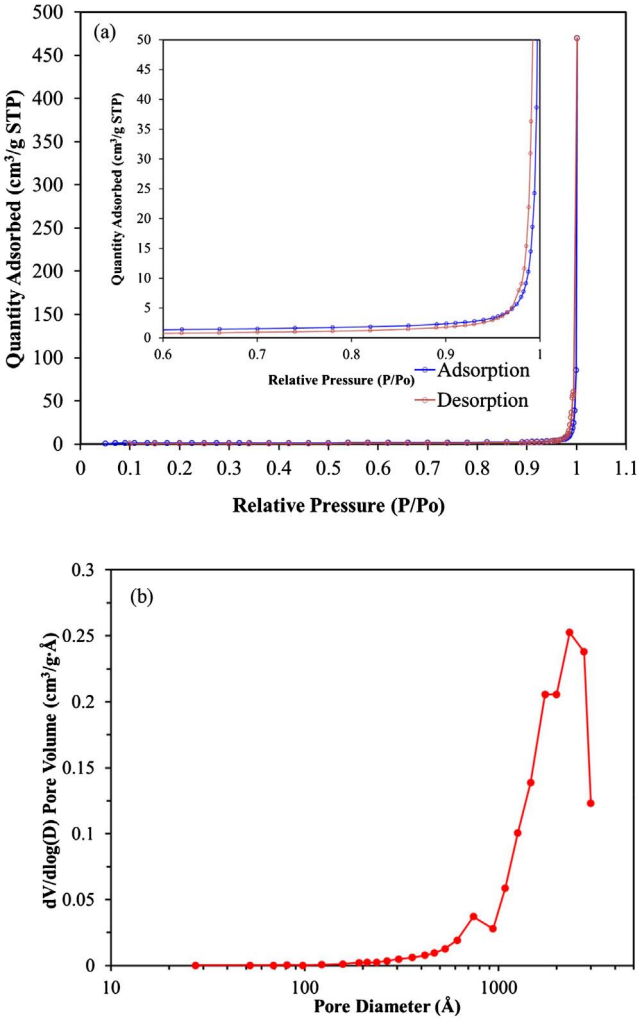

Fig. 6. (a) Nitrogen adsorption-desorption isotherms (inset) and (b) the corresponding pore size distribution curve for BiOCl/o-$PbBiO_2Cl$ (P3BCl-200-13-12).

$PbBiO_2Cl$ and BiOCl absorb only a small amount of visible light. The E_g value of *o*-$PbBiO_2Cl$/BiOCl is determined from a plot of $(\alpha h\nu)^{1/2}$ vs energy ($h\nu$), which is calculated as 2.57 eV.

3.1.6. BET and adsorption-desorption isotherm

From Table 5 and S3–S4, the samples have S_{BET} around 2.67–12.41 m^2/g. However, the results of Table 5 and S3–S4 show that the P5BC1-200-13-12 ($PbBiO_2Cl$/BiOCl) sample—which shows the middle S_{BET}—does represent the highest photocatalytic activity ($k = 2.763 \times 10^{-1}\,h^{-1}$) among the samples, suggesting that the changes in the photocatalytic activity are resulted from $PbBiO_2Cl$/BiOCl composites.

Fig. 6(a) shows the nitrogen adsorption-desorption isotherm curves of $PbBiO_2Cl$/BiOCl. The isotherm of $PbBiO_2Cl$/BiOCl is close to Type III without a hysteresis loop at a highly relative pressure between 0.6 and 1.0 [54]. Fig. 6(b) shows the corresponding pore-size distribution (PSD) of $PbBiO_2Cl$/BiOCl samples. The PSD curve is mono-modal for the samples, indicating large macropores (100–2000 nm). Because the nanoplates (or nanosheets) does not contain pores (Figs. 2(a), 4(e), and S6(e)), the large macropores may reflect porosity within nanoplates (or nanosheets). The large macropores may attribute to the pores formed between stacked nanoplates (or nanosheet), while the large macropores may be ascribed to the pores formed between nanoplates (or nanosheets). Such self-organized porous architectures may be extremely useful in photocatalysis because they provide efficient transport pathways for reactant and product molecules [55]. The pore

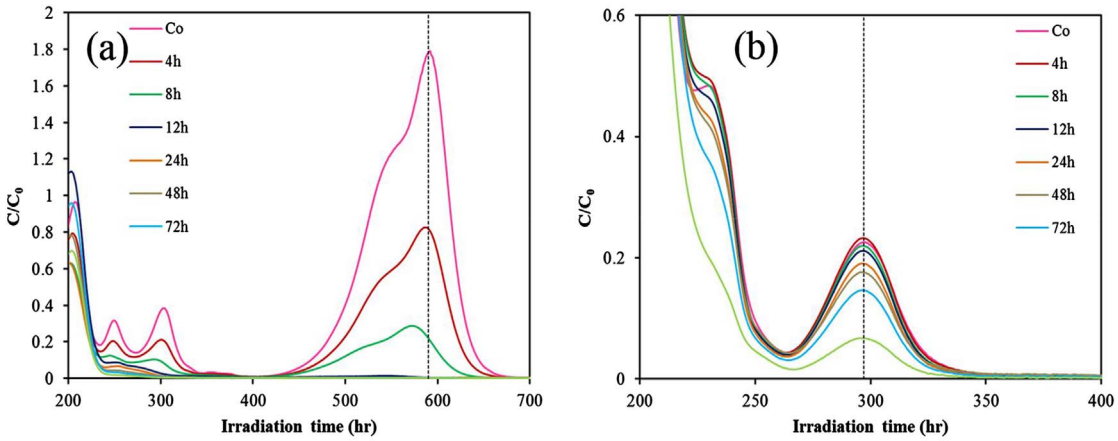

Fig. 7. Photocatalytic activity of BiOCl/o-$PbBiO_2Cl$ (P3BCl-200-13-12) for salicylic acid photocatalytic degradation under visible irradiation.

parameters of the as-prepared samples are summarized in Table 5. The pore volume and size of the $PbBiO_2Cl$/BiOCl composite sample were determined as the pore volume 0.0597 cm^3/g and pore diameter 144.35 nm, respectively.

3.2. Photocatalytic activity

The changes in the UV–vis spectra during the photodegradation of CV and SA in aqueous dispersions of $PbBiO_2Cl$/BiOCl under visible light irradiation are illustrated in Fig. 7. After visible light irradiation for 72 h, approximately 99.5% of CV and approximately 80% of SA are decomposed. In Fig. 7(a), the characteristic absorption band of the CV dye at approximately 588.4 nm decreases rapidly with slightly hypsochromic shifts (555.0 nm); however, no new absorption band appears even in the ultraviolet range ($\lambda > 200$ nm), indicating the possible formation of a series of *N*-de-methylated intermediates and the possible cleavage of the whole conjugated chromophore structure of the CV dye. Further irradiation causes the absorption band at 555.0 nm to decrease; however, no further wavelength shift is observed, suggesting that the band at 555.0 nm is that of the full *N*-de-methylated product of the CV dye [8,9].

The degradation efficiency as a function of reaction time is illustrated in Figs. 8 and S15–S19; the removal efficiency is significantly enhanced in the presence of the as-prepared samples. After the irradiation for 12 h, $PbBiO_2Cl$/BiOCl (P5BC1-200-13-12) exhibits a superior photocatalytic performance, with the CV removal efficiency up to 99%. To further understand the reaction kinetics of CV degradation, the apparent pseudo-first-order model [56] expressed by the equation of $\ln(C_o/C) = kt$ is applied in the experiments. Via the first-order linear fit of the data shown in Table 6, the k value of $PbBiO_2Cl$/BiOCl (P5BC1-200-13-12) is obtained as the maximum degradation rate of $2.763 \times 10^{-1}\ h^{-1}$, which is much higher than that of the other composites; the $PbBiO_2Cl$/BiOCl composite is a much more effective photocatalyst than the others synthesized in this study.

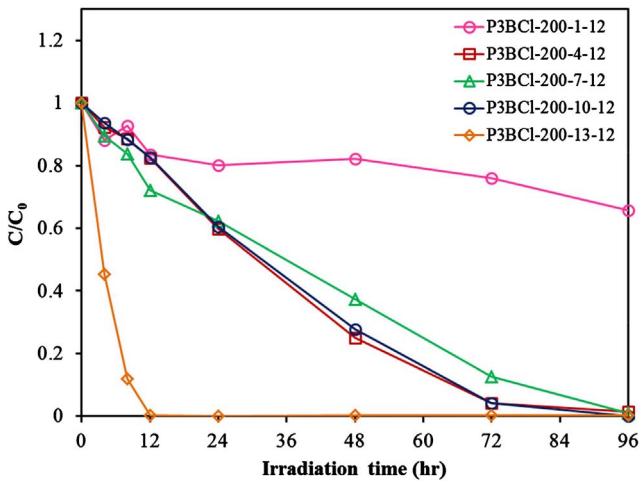

Fig. 8. Photocatalytic activity of BiOCl/o-$PbBiO_2Cl$ (P3BCl-200-13-12) for CV photocatalytic degradation under visible irradiation.

Table 6
Pseudo-first-order rate constants for the degradation of CV with photocatalysts under visible light irradiation.

Samples	K (h^{-1})	R^2	Samples	K (h^{-1})	R^2
P3BCl-150-1-12	0.005	0.91	P1BCl-150-1-12	0.074	0.98
P3BCl-150-4-12	0.013	0.92	P1BCl-150-4-12	0.0135	0.90
P3BCl-150-7-12	0.020	0.94	P1BCl-150-7-12	0.0559	0.97
P3BCl-150-10-12	0.1304	0.95	P1BCl-150-10-12	0.0588	0.97
P3BCl-150-13-12	0.0148	0.90	P1BCl-150-13-12	0.0744	0.97
P3BCl-200-1-12	0.0043	0.93	P1BCl-200-1-12	0.0093	0.92
P3BCl-200-4-12	0.0407	0.95	P1BCl-200-4-12	0.0254	0.90
P3BCl-200-7-12	0.0335	0.91	P1BCl-200-7-12	0.0691	0.97
P3BCl-200-10-12	0.0427	0.93	P1BCl-200-10-12	0.056	0.94
P3BCl-200-13-12	0.2763	0.98	P1BCl-200-13-12	0.0815	0.92
P3BCl-250-1-12	0.0510	0.91	P1BCl-250-1-12	0.006	0.94
P3BCl-250-4-12	0.0042	0.91	P1BCl-250-4-12	0.0081	0.93
P3BCl-250-7-12	0.0583	0.98	P1BCl-250-7-12	0.0547	0.97
P3BCl-250-10-12	0.0541	0.92	P1BCl-250-10-12	0.0549	0.98
P3BCl-250-13-12	0.0444	0.97	P1BCl-250-13-12	0.0389	0.95

It can be assumed that the enhanced photocatalytic activities of composites could be ascribed to a synergistic effect, including high BET surface area, the formation of the heterojunction, layered structure, and low energy band structure. To investigate the BET surface area in the heterostructures, the BET surface area of P3BCl-200-(1-13)-12 samples are measured; the results are shown in Table 5. The lower BET surface areas of P3BCl-200-13-12 (o-$PbBiO_2Cl$/BiOCl) composites suggest that they possess the lower photocatalytic activity. As is known, the photocatalysts are excited to generate electron–hole pairs directly after the illumination in the photocatalytic process. Moreover, the photocatalytic efficiency mainly depends on the recombination rate or the lifetime of the photo-generated electron–hole pairs. The faster recombination occurs, the less time is required for the chemical reactions. Therefore, PL spectra are utilized for investigating the recombination rate of the photogenerated electron–hole pairs. To investigate the separation capacity of the photogenerated carriers in the heterostructures, the PL spectra of P3BCl-200-(1-13)-12 samples are measured; the results are shown in Fig. 10. A strong emission peak around 405 nm appears for the as-prepared samples, which could have been derived from the direct electron–hole recombination of band transitions. However, the characteristic emission peak around the

lowest intensity 405 nm for P3BCl-200-13-12 (o-$PbBiO_2Cl$/BiOCl) indicates that the recombination of photogenerated charge carriers is greatly inhibited. The efficient separation of charge could increase the lifetime of charge carriers and enhance the efficiency of interfacial charge transfer to the adsorbed substrates, thus improving the photocatalytic activity. Comparison of rate constant by different photocatalysts is shown in Table 6. The order of rate constant is as P3BCl-200-13-12 (o-$PbBiO_2Cl$/BiOCl, k = 0.2763) > P3BCl-150-10-12 (o-$PbBiO_2Cl$/BiOCl/PbO, k = 0.1304) > P3BCl-250-13-12 (o-$PbBiO_2Cl$/BiOCl, k = 0.0444) > P3BCl-150-13-12 (o-$PbBiO_2Cl$/BiOCl, k = 0.0148). The photocatalytic activity of the P3BCl-200-13-12 (BiOCl/o-$PbBiO_2Cl$, k = 0.2763) heterojunctons reaches the maximum rate constant of 0.2763 h^{-1}, 6 times higher than that of P3BCl-250-13-12 (o-$PbBiO_2Cl$/BiOCl), 19 times higher than that of P3BCl-150-13-12 (o-$PbBiO_2Cl$/BiOCl), and 2 times higher than that of P3BCl-150-10-12 (o-$PbBiO_2Cl$/BiOCl/PbO). The photocatalytic activity of the o-$PbBiO_2Cl$/BiOCl composites reaches the maximum rate constant 2.763 × 10^{-1} h^{-1}, 3 times higher than that of $PbBiO_2Br$ and 2 times higher than that of BiOCl. Thus, the o-$PbBiO_2Cl$/BiOCl heterojunctons may also play a role in enhancing the photocatalytic activity.

The durability of $PbBiO_2C$ l/BiOCl is evaluated by recycling the used catalyst. After each cycle, the catalyst is collected by centrifugation. No apparent loss is observed in the photocatalytic activity when CV is removed in the 3rd cycle; even during the fifth run, the decline in the photocatalytic activity is 10.2% (Fig. 9(a)). On the other hand, no apparent loss is observed in the photocatalytic activity when 2-hydroxybenzoic acid (salicylic acid; SA) is removed in the 2nd cycle; even during the fifth run, the decline in the photocatalytic activity is 16.3% (Fig. 9(b)). The used $PbBiO_2Cl$/BiOCl is also examined by XRD, and no detectable difference is observed between the as-prepared and the used samples (Fig. 9(c)); hence, $PbBiO_2Cl$/BiOCl has good photostability.

Photocatalysts are excited to generate electron–hole pairs directly after the illumination in the photocatalytic process. Photocatalytic efficiency depends mainly on the recombination rate or the lifetime of the photogenerated electron–hole pairs. The faster the recombination occurs, the shorter the chemical reaction time is. Therefore, PL spectra are utilized for investigating the recombination rate of the photogenerated electron–hole pairs [57]. To investigate the separation capacity of the photogenerated carriers in the heterostructures, the PL spectra of P3BC1-200-1-12 to P3BC1-200-13-12 are measured; the results are shown in Fig. 10. A strong emission peak at approximately 370 nm appears on the as-prepared samples, which could have been derived from the direct electron–hole recombination of band transitions. However, the characteristic emission peak within the low intensity 370 nm for P3BC1-200-1-12 to P3BC1-200-13-12 indicates that the recombination of photogenerated charge carriers is greatly inhibited. The efficient separation of charge could increase the lifetime of charge carriers and enhance the efficiency of interfacial charge transfer to the adsorbed substrates, thus improving the photocatalytic activity [58]. The lowest relative PL intensities of $PbBiO_2Cl$/BiOCl (P5BC1-200-13-12) composites, as shown in Fig. 10, suggesting that they possess a lower recombination rate of electron–hole pairs, resulting in their higher photocatalytic activity, as shown in Fig. 8. The PL results confirm the importance of the composites in hindering the recombination of electrons and holes and explain the reason for the increasing photocatalytic performance of $PbBiO_2Cl$/BiOCl composites.

3.3. Photodegradation mechanism of CV

In general, three possible reaction pathways are assumed to be involved in the photodegradation of organic compounds by a photocatalyst, including (i) photocatalysis, (ii) photolysis, and (iii) dye photosensitization [59]. In the photolysis process, a photoinduced electron on the induced organism directly reacts with O_2 to produce an $^1O_2$ that acts as an oxidant for the photolysis of organism [60]. In the

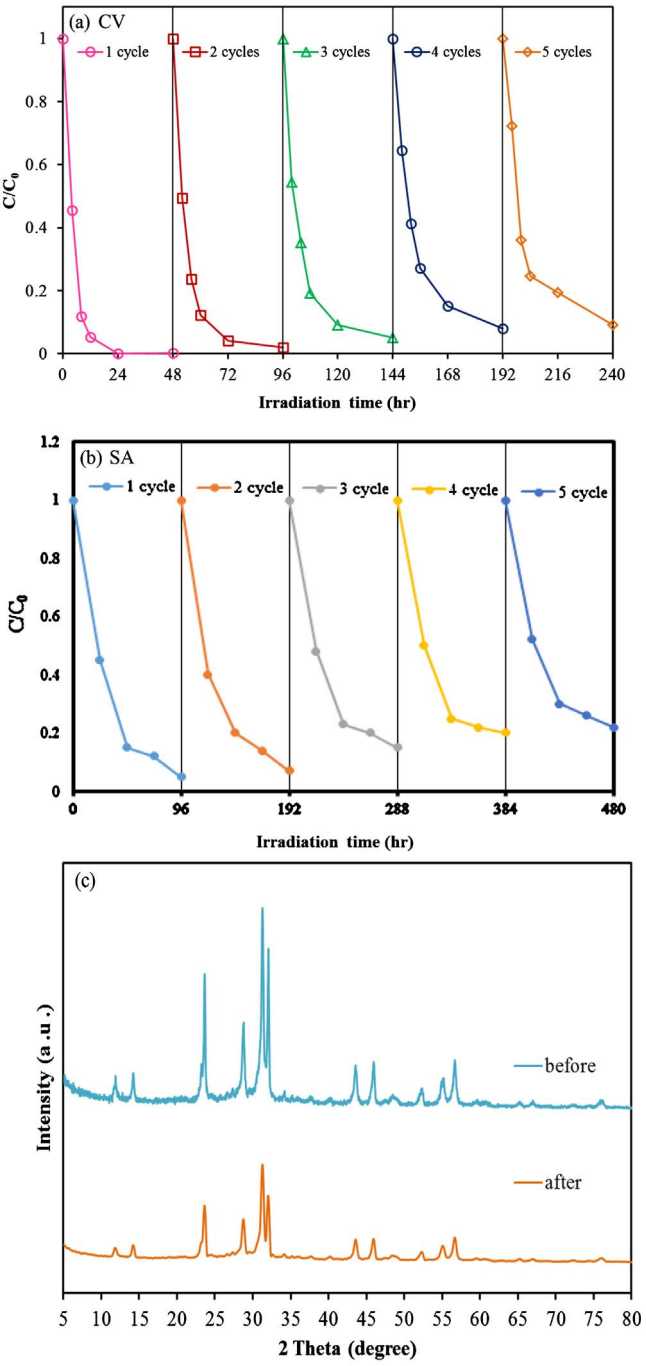

Fig. 9. (a) Cycling runs and (b) XRD patterns acquired before and after the photocatalytic degradation of CV in the presence of P3BC1-200-13-12 ($PbBiO_2Cl$/BiOCl).

experiments, CV degradation induced by photolysis under visible light in a blank experiment is not observable, CV is a structure-stable dye, and the decomposition by the photolysis mechanism is negligible.

As people may know, various primary active species, such as HO·, h^+, O_2^-·, H· and $^1O_2$, could be generated during the photocatalytic degradation reaction in UV–vis/semiconductor systems [60,61]. Dimitrijevic et al. [61] proposed that water, both dissociated on the surface of TiO_2 and in subsequent molecular layers, had a three-fold role of (i) the stabilization of charges, preventing electron-hole recombination, (ii) an electron acceptor, the formation of H atoms in a reaction of photo-generated electrons with protons on the surface, $-OH_2^+$, and (iii) an electron donor, the reaction of water with photo-generated holes to give ·OH radicals. Ma et al. revealed that O_2^-· was the main active

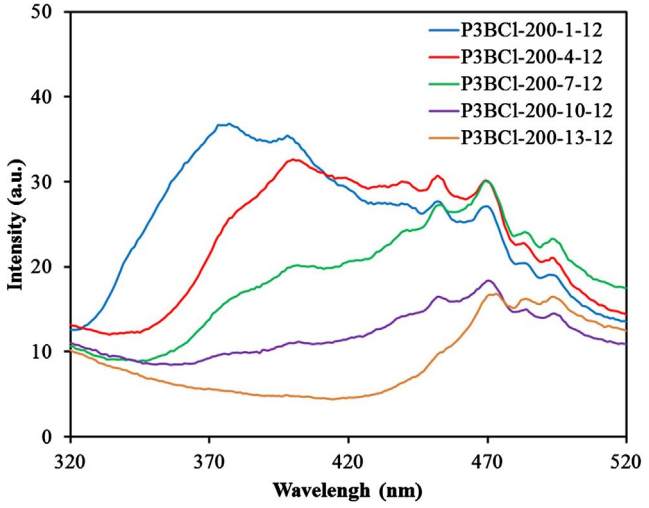

Fig. 10. Photoluminescence (PL) spectra of the as-prepared photocatalysts under different pH values and reaction temperature. (Molar ratio $Pb(NO_3)_2/Bi(NO_3)_3$ = 3/3, KCl = 1 mmol, reaction time 12 h).

species for NO oxidation to NO_3^- with TO_2/g-C_3N_4 under visible and UV light [62]. Zou's group illustrated a typical Cu_2O–reduced graphene oxide photocatalyst being favorable for the production of $O_2^-\cdot$ reactive species for methylene blue [63]. Jiang et al. revealed that the photogenerated h^+ and $O_2^-\cdot$ were the main oxidative species for the degradation of methyl orange [64]. The generation of $O_2^-\cdot$ could not only inhibit the recombination of photoinduced charge carriers but also benefit the de-chlorination of chlorinated phenol derivative. The hydroxyl radical HO might only be formatted via an $e^- \rightarrow O_2^-\cdot \rightarrow H_2O_2 \rightarrow \cdot OH$ route. Meanwhile, ·OH radicals were formatted by multistep $O_2^-\cdot$ reduction in the system [65]. Kondrakov et al. reported the study on the photocatalytic generation of free OH radicals ($\cdot OH_{free}$) in aqueous TiO_2 suspensions using an ^{18}O isotope labeling and a "remote" photocatalysis approach. A probe compound, 1,3,5-trichlorobenzene (TCB), was adsorbed in pores of silica gel (SG) microparticles to be shielded from the direct hole oxidation [66]. According to earlier studies 63], the photocatalytic process was mainly governed by $O_2^-\cdot$, rather than by ·OH, e^- or h^+. In earlier study, CV photodegradation by BiO_mX_n/BiO_pX_q (X, Y = Cl, Br, I) under visible light was dominated by $O_2^-\cdot$ oxidation being the main active species and ·OH and h^+ being the minor active species [65,67]. On the basis of the references presented above, it is proposed that the probability of forming ·OH should be much lower than that for $O_2^-\cdot$; however, ·OH is an extremely strong and nonselective oxidant, which leads to the partial or complete mineralization of several organic chemicals.

In order to evaluate the effect of the active species during the photocatalytic reaction, EPR measurement is used for scavenging the relevant active species. From Fig. 11, not only are the characteristic peaks of DMPO-·OH adducts observed, but the characteristic peaks of the DMPO-$O_2^-\cdot$ adducts are also observed under visible light irradiated $PbBiO_2Cl$/BiOCl suspension. Fig. 11(a), (b) shows that no EPR signal is observed when the reaction is performed in the dark, while the signals with the intensity corresponding to the characteristic peak of DMPO-·OH and DMPO-$O_2^-\cdot$ adducts [68] are observed during the reaction process under visible light irradiation, and the intensity gradually increases with the prolonged reaction time, suggesting that $O_2\cdot^-$ and OH being active species are formed in the presence of $PbBiO_2Cl$/BiOCl and oxygen under visible light irradiation.

In order to re-evaluate the effect of the active species during the photocatalytic reaction, different quenchers are used for scavenging the relevant active species. As shown in Fig. 11(c), the photocatalytic degradation of CV is obviously affected by the addition of SA, AO, BQ, and IPA quenching decreases evidently compared with that of no-

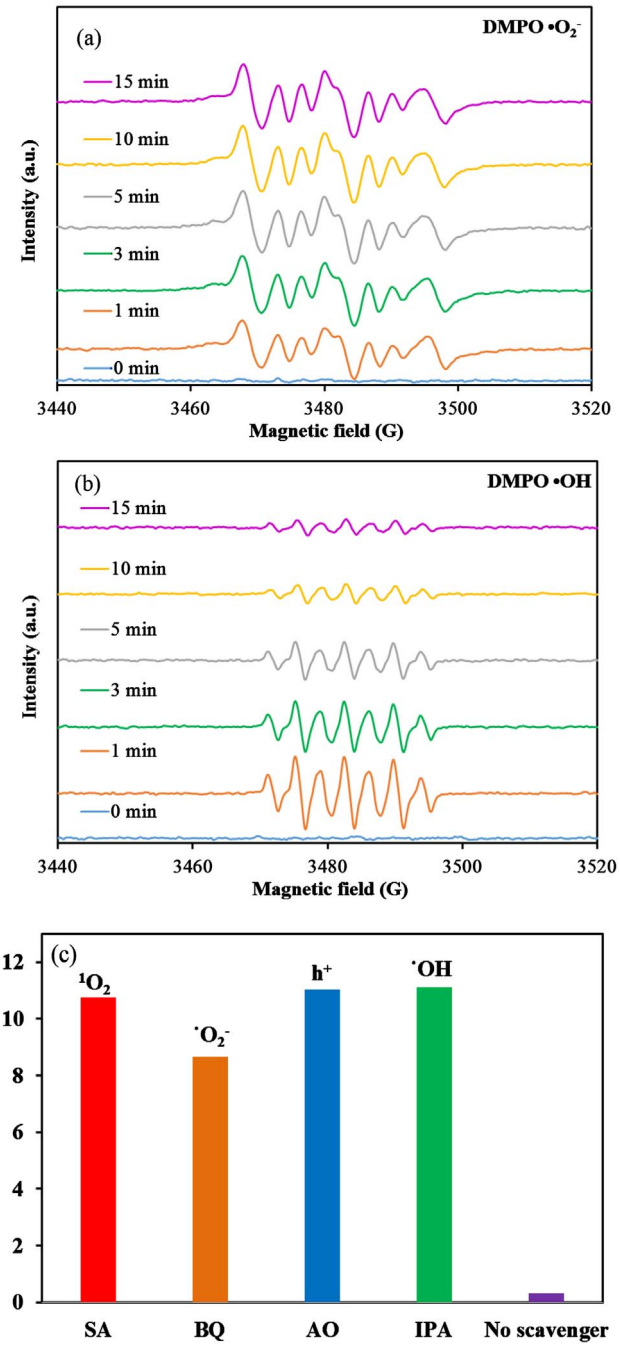

Fig. 11. DMPO spin-trapping EPR spectra for (a) DMPO-·O_2^- and (b) DMPO-·OH under visible light irradiation with P5B3-200-10-12 (BiOCl/o-$PbBiO_2Cl$). (c) Photodegradation of CV dye BiOCl/o-$PbBiO_2Cl$ (P3BCl-200-13-12) in the presence of different scavengers under solar light irradiation.

quenching, indicating that $O_2\cdot^-$, ·OH, h^+, and $^1O_2$ are the major active species in the mechanism of photocatalytic degradation of CV. Hence, the quenching effects of scavengers and EPR illustrate that the reactive $O_2\cdot^-$, ·OH, h^+, and $^1O_2$ play the major role in the photocatalytic degradation of CV.

The structure characterizations have proven that $PbBiO_2Cl$/BiOCl is a two-phase heterojunction. Considering that the heterojunction presents much higher photocatalytic activities than the component phase alone, it is reasonable that there might be synergetic effect between $PbBiO_2Cl$ and BiOCl. Actually, many researchers have noted the synergetic effect in heterojunction systems consisting of two semiconductors in contact [69,70] and attributed the effect to the efficient

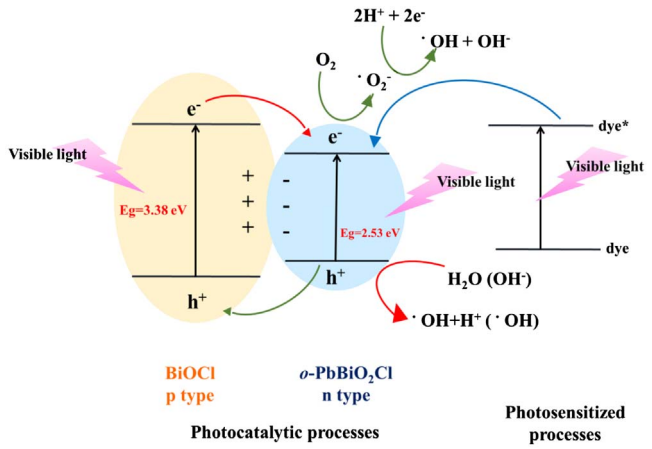

Fig. 12. Schematic illustration of the band gap structures of P3BC1-200-13-12 ($PbBiO_2Cl$/BiOCl).

charge transfer at the interface of two semiconductors, which would result in an effective photoexcited electron–hole separation and, consequently, enhance the photocatalytic activity. The driving force of charge transfer originates from the matching band potentials. Therefore, the suitable band potential is the precondition for the synergetic effect of heterojunction photocatalysts. Typically for V_2O_5/$BiVO_4$ heterostructured photocatalysts [71], the conduction-band (CB) potential level of $BiVO_4$ is more negative than that of V_2O_5 so that photogenerated electrons could migrate from $BiVO_4$ to V_2O_5 driven by the contact electric field. Fig. 12 shows the type-I heterostructure band alignment [70] and the valence-band (VB) XPS spectra of $PbBiO_2Cl$ and BiOCl. In the type-I band alignment, both VB and CB edges of $PbBiO_2Cl$ are localized within the energy gap of BiOCl, forming the straddling band alignment (Fig. 12). The VB and CB potentials of two different semiconductors play a crucial role in the determination of the physical features of photogenerated charges and the photocatalytic performance. $PbBiO_2Cl$/BiOCl heterojunction photocatalysts, the CB potential level of BiOCl, are more negative than that of $PbBiO_2Cl$ so that photogenerated electrons could migrate from BiOCl to $PbBiO_2Cl$ driven by the contact electric field. As the CB potentials of BiOCl (0.39 eV) and $PbBiO_2Cl$ (0.93 eV) are a little different, the photoexcited electron is easy to transfer from the CB of BiOCl to the CB of $PbBiO_2Cl$; and, the VB potentials of BiOCl (3.77 eV) and $PbBiO_2Cl$ (3.46 eV) are also a little different that the photoexcited holes are easy to transfer from the VB of BiOBr to the VB of $PbBiO_2Cl$. Therefore, $PbBiO_2Cl$/BiOCl photocatalysts show great increase in the separation extent and lifetime of the photogenerated electrons, leading to the effective photodegradation of CV under visible light irradiation.

The generation of $O_2^{-}\cdot$ could not only inhibit the recombination of photoinduced charge carriers but also benefit the degradation of CV. The hydroxyl radical HO might be formatted by an $e^- \rightarrow O_2^{-}\cdot \rightarrow H_2O_2 \rightarrow \cdot OH$ route and/or h^+ with OH^- and H_2O species [72]. On the basis of above reports, a proposed mechanism of degradation is illustrated in Fig. 12. Once the electron and the hole reach the CB and the VB of $PbBiO_2Cl$, it induces the formation of active oxygen species, which cause the degradation of CV. It is clear that, except for the photodegradation of CV by the route of $PbBiO_2Cl$/BiOCl-mediated and photosensitized processes, another type of photocatalytic route accounts for the enhanced photocatalytic activity. In Fig. 12, both the photosensitized and photocatalytic processes are preceded concurrently. However, in photosensitized and photocatalytic processes, $O_2\cdot^-$ radicals are generated by the reaction of photogenerated and photosensitized electrons with oxygen gas on the photocatalyst surface, and ·OH radicals are also generated by the reaction of $O_2\cdot^-$ radicals with H^+ ion, $^1O_2$ with electron, and hole h^+ with OH^- ion (or H_2O). These cycles continuously occur when the system is exposed to visible-light irradiation [65]; and, after several cycles of photo-oxidation, the degradation of CV by the produced oxidant species can be expressed by Eqs. (11)–(12).

$$CV + O_2^{-}/OH/h^+/^1O_2 \rightarrow \text{degraded compounds} \quad (11)$$

$$(12)\ CV^{+}\cdot + O_2^{-}/OH/h^+/^1O_2 \rightarrow \text{degraded compounds}$$

In a visible-light-induced semiconductor system, hydroxylated compounds were also identified for the photocatalytic degradation of CV [65,67]. In earlier reports [72,73], the *N*-de-alkylation processes were preceded by the generation of a nitrogen-centered radical, and the destruction of the dye chromophore structure was preceded by the formation of a carbon-centered radical in the photocatalytic degradation of CV dye under UV or visible light irradiation. The reaction mechanisms for $PbBiO_2Cl$/BiOCl-mediated photocatalytic processes proposed in this research should offer some notion for the applications to the decoloration of dyes.

4. Conclusions

The $PbBiO_2Cl$/BiOCl heterojunctions have been synthesized by using template-free hydrothermal methods for the first time. The $PbBiO_2Cl$/BiOCl heterojunctions show the type-I heterostructure band alignment. The removal efficiency is significantly enhanced in the presence of $PbBiO_2Cl$/BiOCl. The increased photocatalytic activities of $PbBiO_2Cl$/BiOCl could be attributed to the formation of the heterojunction between $PbBiO_2Cl$ and BiOCl, which effectively suppresses the recombination of photo-generated electron–hole pairs. It can be concluded that the enhanced photocatalytic activities of $PbBiO_2Cl$/BiOCl materials could be owe to the formation of the heterojunction. The quenching effects of scavengers and EPR illustrate that the reactive $O_2\cdot^-$, ·OH, h^+, and $^1O_2$ play the major role in the photocatalytic degradation of CV. This work is useful for the synthesis of $PbBiO_2Cl$/BiOCl and the photocatalytic degradation of CV in future applications to environmental pollution and control.

Acknowledgment

This research was supported by the Ministry of Science and Technology of the Republic of China (MOST-105-2119-M-142-001).

Appendix A. Supplementary data

Supplementary data associated with this article can be found, in the online version, at http://dx.doi.org/10.1016/j.cattod.2017.04.030.

References

[1] M.R. Hoffmann, S.T. Martin, W. Choi, D.W. Bahnemann, Chem. Rev. 95 (1995) 69–96.
[2] M. Urbani, M. Grätzel, M.K. Nazeeruddin, T. Torres, Chem. Rev. 114 (2014) 12330–12396.
[3] A. Kubacka, M. Fernández-García, G. Colón, Chem. Rev. 112 (2012) 1555–1614.
[4] D.F. Duxbury, Chem. Rev. 93 (1993) 381–433.
[5] B.P. Cho, T. Yang, L.R. Blankenship, J.D. Moody, M. Churchwell, F.A. Bebland, S.J. Culp, Chem. Res. Toxicol. 16 (2003) 285–294.
[6] S.Y. Chou, C.C. Chen, L.W. Chen, Y.M. Dai, J.H. Lin, W.W. Lee, RSC Adv. 6 (2016) 33478–33491.
[7] S.Y. Chou, W.H. Chung, L.W. Chen, Y.M. Dai, W.Y. Lin, J.H. Lin, C.C. Chen, RSC Adv. 6 (2016) 82743–82758.
[8] H.P. Lin, C.C. Chen, W.W. Lee, Y.Y. Lai, J.Y. Chen, Y.Q. Chen, J.Y. Fu, RSC Adv. 6 (2016) 2323–2336.
[9] S.T. Huang, Y.R. Jiang, S.Y. Chou, Y.M. Dai, C.C. Chen, J. Mol. Catal. A: Chem. 391 (2014) 105–120.
[10] H.P. Lin, W.W. Lee, S.T. Huang, L.W. Chen, T.W. Yeh, J.Y. Fu, C.C. Chen, J. Mol. Catal. A: Chem. 417 (2016) 168–183.
[11] K. Yu, S. Yang, C. Liu, H. Chen, H. Li, C. Sun, S.A. Boyd, Environ. Sci. Technol. 46 (2012) 7318–7326.
[12] W.L.W. Lee, J.S. Lin, J.L. Chang, J.Y. Chen, M.C. Cheng, C.C. Chen, J. Mol. Catal. A: Chem. 361–362 (2012) 80–90.
[13] Y. He, H. Huang, Y. Zhang, X. Li, N. Tian, Y. Guo, Y. Luo, Mater. Res. Bull. 64 (2015) 405–409.

[14] S. Füldner, P. Pohla, H. Bartling, S. Dankesreiter, R. Stadler, M. Gruber, A. Pfitzner, B. König, Green Chem. 13 (2011) 640–643.
[15] C. Yu, Z. Wu, R. Liu, D.D. Dionysiou, K. Yang, C. Wang, H. Liu, Appl. Catal. B: Environ. 209 (2017) 1–11.
[16] H. Huang, K. Xiao, Y. He, T. Zhang, F. Dong, X. Du, Y. Zhang, Appl. Catal. B: Environ. 199 (2016) 75–86.
[17] B. Wang, J. Di, P. Zhang, J. Xia, S. Dai, H. Li, Appl. Catal. B: Environ. 206 (2017) 127–135.
[18] J. Kou, C. Lu, J. Wang, Y. Chen, Z. Xu, R.S. Varma, Chem. Rev. 117 (2017) 1445–1514.
[19] W.J. Ong, L.L. Tan, Y.H. Ng, S.T. Yong, S.P. Chai, Chem. Rev. 116 (2016) 7159–7329.
[20] D.O. Charkin, P.S. Berdonosov, V.A. Dolgikh, P. Lightfoot, J. Solid State Chem. 175 (2003) 316–321.
[21] A.M. Kusainova, P. Lightfoot, W. Zhou, Chem. Mater. 13 (2001) 4731–4737.
[22] S.M. Fray, C.J. Milne, P. Lightfoot, J. Solid State Chem. 128 (1997) 115.
[23] A.M. Kusainova, W. Zhou, J.T.S. Irvine, P. Lightfoot, J. Solid State Chem. 166 (2002) 148.
[24] J.F. Ackerman, Mater. Res. Bull. 17 (1982) 883–886.
[25] M. Batuk, D. Batuk, A.A. Tsirlin, D.S. Filimonov, Chem. Mater. 27 (2015) 2946–2956.
[26] F.J. Maile, G. Pfaff, P. Reynders, Prog. Org. Coat. 54 (2005) 150.
[27] Y.H. Liao, J.X. Wang, J.S. Lin, W.H. Chung, W.Y. Lin, C.C. Chen, Catal. Today 174 (2011) 148–159.
[28] Z. Chen, H. Jiang, W. Jin, C. Shi, Appl. Catal. B: Environ. 180 (2016) 698–706.
[29] J.A. Seabold, K.S. Choi, J. Am. Chem. Soc. 134 (2012) 2186–2192.
[30] H. Cheng, B. Huang, Y. Dai, Nanoscale 6 (2014) 2009–2026.
[31] L. Ye, J. Chen, L. Tian, J. Liu, T. Penga, K. Deng, L. Zan, Appl. Catal. B: Environ. 130–131 (2013) 1–7.
[32] Y.R. Jiang, H.P. Lin, W.H. Chung, Y.M. Dai, W.Y. Lin, C.C. Chen, J. Hazard. Mater. 283 (2015) 787–805.
[33] W. Wei, Y. Dai, B.B. Huang, J. Phys. Chem. C 113 (2009) 5658–5663.
[34] F.Y. Xiao, J. Xing, L. Wu, Z.P. Chen, X.L. Wang, H.G. Yang, RSC Adv. 3 (2013) 10687–10690.
[35] Y. Yu, Y. Gu, W. Zheng, Y. Ding, Y. Cao, J. Phys. Chem. C 119 (2015) 28190–28193.
[36] Z. Shan, W. Wang, X. Lin, H. Ding, F. Huang, J. Solid State Chem. 181 (2008) 1361–1366.
[37] S. Rau, B. Schäfer, D. Gleich, E. Anders, M. Rudolph, M. Friedrich, H. Görls, W. Henry, J.G. Vos, Angew. Chem. 118 (2006) 6361–6364.
[38] A. Pfitzner, P. Pohla, Z. Anorg. Allg. Chem. 635 (2009) 1157–1159.
[39] H. Xie, C. Jia, Y. Jiang, X. Wang, Mater. Chem. Phys. 133 (2012) 1003–1005.
[40] C. He, M. Gu, Scripta Mater. 55 (2006) 481–484.
[41] J.D.Y. Liu, X. Pan, Y. Zhang, J. Yu, K. Nakajim, H. Taniguchi, Catal. Commun. 39 (2013) 65–69.
[42] X. Li, J. Wang, D. Xu, Z. Sun, Q. Zhao, W. Peng, Y. Li, G. Zhang, F. Zhang, X. Fan, ACS Sustain. Chem. Eng. 3 (2015) 1017–1022.
[43] P. Wang, B. Huang, X. Qin, X. Zhang, Y. Dai, J. Wei, M.H. Whangbo, Angew. Chem. Int. Ed. 47 (2008) 7931–7933.
[44] L.S. Zhang, K.H. Wong, H.Y. Yip, C. Hu, J.C. Yu, C.Y. Chan, P.K. Wong, Environ. Sci. Technol. 44 (2010) 1392–1398.
[45] M.C. Yin, Z.S. Li, J.H. Kou, Z.G. Zou, Environ. Sci. Technol. 43 (2009) 8361–8366.
[46] S.G. Meng, D.Z. Li, M. Sun, W.J. Li, J.X. Wang, J. Chen, X.Z. Fu, G.C. Xiao, Catal. Commun. 12 (2011) 972–975.
[47] G. Li, K.H. Wong, X. Zhang, C. Hu, J.C. Yu, R.C.Y. Chan, P.K. Wong, Chemosphere 76 (2009) 1185–1191.
[48] H.L. Chen, W.W. Lee, W.H. Chung, H.P. Lin, Y.J. Chen, Y.R. Jiang, W.Y. Lin, C.C. Chen, J. Taiwan Inst. Chem. Eng. 45 (2014) 1892–1909.
[49] M.M. Rahman, K.M. Krishna, T. Soga, T. Jimbo, M. Umeno, J. Phys. Chem. Solid 60 (1999) 201–210.
[50] A.I. Kovalev, D.L. Wainstein, A.Y. Rashkovskiy, A. Osherov, Y. Golan, Surf. Interface Anal. 42 (2010) 850–854.
[51] N.B. Rahna, V. Kalarivalappil, M. Nageri, S.C. Pillai, S.J. Hinder, V. Kumar, B.K. Vijayan, Mater. Sci. Semicon. Proc. 42 (2016) 303–310.
[52] Y.R. Jiang, S.Y. Chou, J.L. Chang, S.T. Huang, H.P. Lin, C.C. Chen, RSC Adv. 5 (2015) 30851–30860.
[53] S.T. Huang, Y.R. Jiang, S.Y. Chou, Y.M. Dai, C.C. Chen, J. Mol. Catal. A: Chem. 391 (2014) 105–120.
[54] L. Lin, S. Yuan, J. Chen, L. Wang, J. Wan, X. Lu, Chemosphere 78 (2010) 66–71.
[55] F. Dong, Y. Sun, M. Fu, Z. Wu, S.C. Lee, J. Hazard. Mater. 219–220 (2012) 26–34.
[56] A. Chatzitakis, C. Berberidou, I. Paspaltsis, G. Kyriakou, T. Sklaviadis, I. Poulios, Water Res. 42 (2008) 386–394.
[57] K. Ishibashi, A. Fujishima, T. Watanabe, K. Hashimoto, Electrochem. Commun. 2 (2000) 207–210.
[58] F. Dong, Y. Sun, M. Fu, Z. Wu, S.C. Lee, J. Hazard. Mater. 219–220 (2012) 26–34.
[59] C. Nasr, K. Vinodgopal, L. Fisher, S. Hotchandani, A.K. Chattopadhyay, P.V. Kamat, J. Phys. Chem. 100 (1996) 8436–8442.
[60] X. Xiao, R. Hao, M. Liang, X. Zuo, J. Nan, L. Li, W. Zhang, J. Hazard. Mater. 233–234 (2012) 122–130.
[61] N.M. Dimitrijevic, B.K. Vijayan, O.G. Poluektov, T. Rajh, K.A. Gray, H. He, P. Zapol, J. Am. Chem. Soc. 133 (2011) 3964–3971.
[62] J. Ma, C. Wang, H. He, Appl. Catal. B: Environ. 184 (2016) 28–34.
[63] W. Zou, L. Zhang, L. Liu, X. Wang, J. Sun, S. Wu, Y. Deng, C. Tang, F. Gao, L. Dong, App. Catal. B: Environ. 181 (2016) 495–503.
[64] D. Jiang, J. Li, C. Xing, Z. Zhang, S. Meng, M. Chen, ACS Appl. Mater. Interfaces 7 (2015) 19234–19242.
[65] Y. Tian, B. Chang, J. Lu, J. Fu, F. Xi, X. Dong, ACS Appl. Mater. Interfaces 5 (2013) 7079–7085.
[66] A.O. Kondrakov, A.N. Ignatev, V.V. Lunin, F.H. Frimmel, S. Bräse, H. Horn, Appl. Catal. B: Environ. 182 (2016) 424–430.
[67] W.W. Lee, C.S. Lu, C.W. Chuang, Y.J. Chen, J.Y. Fu, C.W. Siao, C.C. Chen, RSC Adv. 5 (2015) 23450–23463.
[68] X. Xiao, C. Xing, G. He, X. Zuo, J. Nan, L. Wang, Appl. Catal. B: Environ. 148–149 (2014) 154–163.
[69] H. Li, Y. Zhou, W. Tu, J. Ye, Z. Zou, Adv. Funct. Mater. 25 (2015) 998–1013.
[70] Z. Li, J. Feng, S. Yan, Z. Zou, Nano Today 10 (2015) 468–486.
[71] J. Su, X.X. Zou, G.D. Li, X. Wei, C. Yan, Y.N. Wang, J. Zhao, L.J. Zhou, J.S. Chen, J. Phys. Chem. C 115 (2011) 8064.
[72] H.J. Fan, C.S. Lu, W.L.W. Lee, M.R. Chiou, C.C. Chen, J. Hazard. Mater. 185 (2011) 227–235.
[73] S. Ameen, M.S. Akhtar, M. Nazim, H.S. Shin, Mater. Lett. 96 (2013) 228–232.